Received: 12 March 2026 | Revised: 14 May 2026 | Accepted: 17 July 2026 | Published online: 20 August 2026

Journal of Optics and Photonics Research
2026, Vol. 00(00) 1–15
DOI: 10.47852/bonviewJOPR62029619
BON VIEW PUBLISHING

RESEARCH ARTICLE

Optomechanical Response Analysis of a Tunable Monolithic Littrow WDM System Under Different Mechanical Boundary Conditions

Mehdi Kharazmi[1], Pierre Pottier[1, 2], Jayan Ozhikandathil[1] and Muthukumaran Packirisamy[1,*]

[1] *Optical-Bio Microsystems Laboratory, Concordia University, Canada*

[2] *Aeponyx Enterprises Inc., Canada*

Abstract: We present a comparative optomechanical analysis of a tunable, monolithic Littrow wavelength-division multiplexer (WDM) integrating silicon nitride waveguides with an enhanced concave diffraction grating. Three device configurations, distinguished by their mechanical boundary conditions and actuation locations, are investigated using coupled finite-element mechanical modeling and full-wave electromagnetic simulations. The analysis establishes quantitative relationships between applied force, structural deformation, and spectral tuning across the extended C-band. Results show that structural stiffness strongly governs the tuning behavior. The fixed–fixed configuration provides highly linear wavelength tuning, stable channel spacing, and minimal mechanical displacement but requires significantly higher actuation forces. In contrast, the fixed–free and fixed–anchored–free configurations reduce structural stiffness, nearly doubling the wavelength sensitivity to the applied force, though with mild nonlinearity and increased displacement. These configurations also partially restore near-linear spectral behavior. Across all configurations, a clear trade-off emerges between mechanical compliance, tuning sensitivity, and structural stability. Increasing compliance reduces the required actuation force and improves tuning sensitivity but requires larger actuator travel and may affect mechanical reliability. These findings provide quantitative design guidelines for optimizing mechanical boundary conditions and actuator strategies in compact, energy-efficient, and low-loss monolithic microelectromechanical systems–photonic WDM systems.

Keywords: tunable wavelength-division multiplexer, monolithic coupled system, concave diffraction grating, MEMS-based photonic integrated device, Littrow configuration

1. Introduction

1.1. Background

The rapid growth of global data traffic, driven by cloud computing, the Internet of Things, and artificial intelligence, has created an urgent demand for high-capacity, energy-efficient optical communication networks. Global internet traffic is projected to continue increasing at compound annual growth rates exceeding 25%, placing unprecedented pressure on optical communication infrastructure. Addressing this challenge requires photonic technologies that combine high bandwidth, a compact footprint, and low power consumption [1, 2].

Integrated photonic platforms enable a broad range of potential high-speed optical components, including waveguides, couplers, modulators, splitters, and detectors. Their integration with microelectromechanical systems (MEMS) further extends functionality by enabling reconfigurable and programmable optical devices. MEMS-based photonics provide precise mechanical control with low static power consumption, making them suitable for continuously tunable applications [3–6].

Silicon photonics has emerged as a dominant platform for large-scale integration due to its compatibility with CMOS fabrication and high integration density. However, conventional silicon-on-insulator (SOI) platforms can suffer from elevated optical losses and fabrication constraints in some applications. Silicon nitride (SiN) has gained increasing attention as an alternative material system, offering ultra-low propagation loss, broad transparency, and excellent thermal stability, making it ideal for wavelength-selective and tunable photonic devices [7, 8].

Wavelength-division multiplexing (WDM) is a key technology for increasing optical fiber capacity by enabling multiple wavelength channels on a single fiber [1, 9]. As networks evolve toward greater flexibility and programmability, interest is growing in compact, tunable, and energy-efficient WDM devices for dynamic spectral reconfiguration. Various on-chip approaches have been explored, including thin-film filters, arrayed

*Corresponding author: Muthukumaran Packirisamy, Optical-Bio Microsystems Laboratory, Concordia University, Canada. Email: pmuthu@alcor.concordia.ca

waveguide gratings (AWGs), ring resonators, and MEMS-based filters, though they often involve trade-offs among tuning range, insertion loss, power consumption, and scalability [10–12].

Concave diffraction gratings (CDGs) offer an alternative by combining wavelength selectivity with the focusing properties of curved mirrors [13–16]. CDG-based WDMs enable compact footprints, high efficiency, and broadband operation. Bragg-mirror-enhanced CDGs further improve efficiency and reduce size, making them attractive for integrated WDM systems [14]. A comparison of representative WDM technologies is given in Table 1 [17].

MEMS-actuated CDG-based photonic devices enable dynamic wavelength tuning through controlled mechanical displacement [3, 6]. MEMS photonic systems are commonly classified as gap-separated or monolithic. Gap-separated architectures introduce optical gaps that reduce mechanical constraints and enable large displacement under relatively low actuation forces [17]. In contrast, monolithic systems maintain continuous waveguides, eliminating coupling interfaces and reducing insertion loss [24]. These characteristics improve optical stability, robustness, and wavelength-routing predictability. As a result, monolithic architectures are particularly attractive for tunable WDM systems [25, 26].

However, the rigid mechanical coupling inherent in monolithic platforms increases structural stiffness and requires deformation of the waveguide–slab–CDG structure during tuning. Consequently, the spectral response becomes strongly dependent on boundary conditions and actuation location, directly affecting displacement behavior, wavelength tuning, and optical stability. Although previous studies have explored MEMS-tunable photonic devices and compliant photonic architectures [17], the influence of mechanical boundary conditions on the optomechanical response of monolithic WDM systems has not yet been systematically investigated.

In this work, we investigate mechanically tunable monolithic WDM systems based on a three-waveguide Littrow architecture integrating silicon nitride waveguides with an enhanced CDG. Three configurations with different mechanical boundary conditions are analyzed under actuation, and their deformation, required force, and spectral response are systematically correlated across the 1538–1562 nm C-band. The study establishes quantitative relationships among structural stiffness, wavelength tuning, spectral linearity, and channel-spacing stability. These results reveal the trade-offs between tuning sensitivity, mechanical deformation, and optical performance. The results provide predictive design guidelines for compact, low-loss, and energy-efficient monolithic MEMS–photonic WDM systems.

1.2. System overview

The system investigated in this work is a mechanically tunable, monolithic wavelength-division multiplexer based on a Littrow-configuration CDG integrated with silicon nitride (SiN) waveguides. The architecture is designed to enable systematic evaluation of how mechanical boundary conditions and applied forces influence the optical spectral behavior of a monolithic WDM device (Figure 1).

The trapezoidal slab waveguide is defined in the x–z plane, where z denotes the optical propagation direction and x represents the lateral extent of the slab, while the y-direction corresponds to the out-of-plane dimension. Throughout this work, x is also defined as the in-plane actuation direction, z as the optical propagation direction, and y as the out-of-plane dimension.

The proposed architecture is compatible with established silicon nitride photonic and MEMS fabrication processes. The SiN waveguides are embedded in SiO_2 cladding on an SOI-based MEMS platform and can be realized using standard deposition, lithography, etching, and sacrificial release techniques. Although fabrication tolerances are not explicitly modeled, the design provides a practical foundation for future experimental implementation.

1.2.1. *Optical design*

The photonic subsystem comprises three parallel SiN access waveguides embedded in silica and coupled to a trapezoidal slab that guides light to an enhanced CDG. In Rowland geometry, the CDG diffracts and refocuses light into three wavelength-dependent output channels centered at 1538 nm, 1550 nm, and 1562 nm, with 12 nm spacing across the C-band.

Silicon nitride provides low loss, broad transparency, and high thermal stability, ensuring that spectral variations primarily result from mechanical actuation. The Littrow configuration provides a compact footprint and high wavelength selectivity, making it well suited for systematic optomechanical tuning analysis.

Table 1
Performance comparison of recent WDM technologies

Technology	Tuning range	Tuning mechanism	Insertion loss (dB)	Footprint	Actuation power/force	Reconfigurable
Arrayed Waveguide Grating, AWG [10, 18, 19]	1–2 nm	Passive interference/ electrothermal	<5	Large (mm^2-cm^2)	>10 mW	No
Inverse Design [20, 21]	–	Passive interference	<3	Ultra-Compact	–	No
Ring Resonator [12, 22]	1–10 nm	Electrostatic/ thermal	<1	Compact (<0.1 mm^2)	1–20 mW/µN-mN	Yes
MEMS Fabry-Perot Filters [23]	20–50 nm	MEMS	<3	Moderate	µN-mN	Yes
Monolithic Coupled CDG [24]	30–60 nm	MEMS	<1	Moderate	mN	Yes

Figure 1
Schematic of the monolithic MEMS–photonic WDM device with a concave diffraction grating (CDG); the inset shows the cross-sectional view and (b) top view of the device

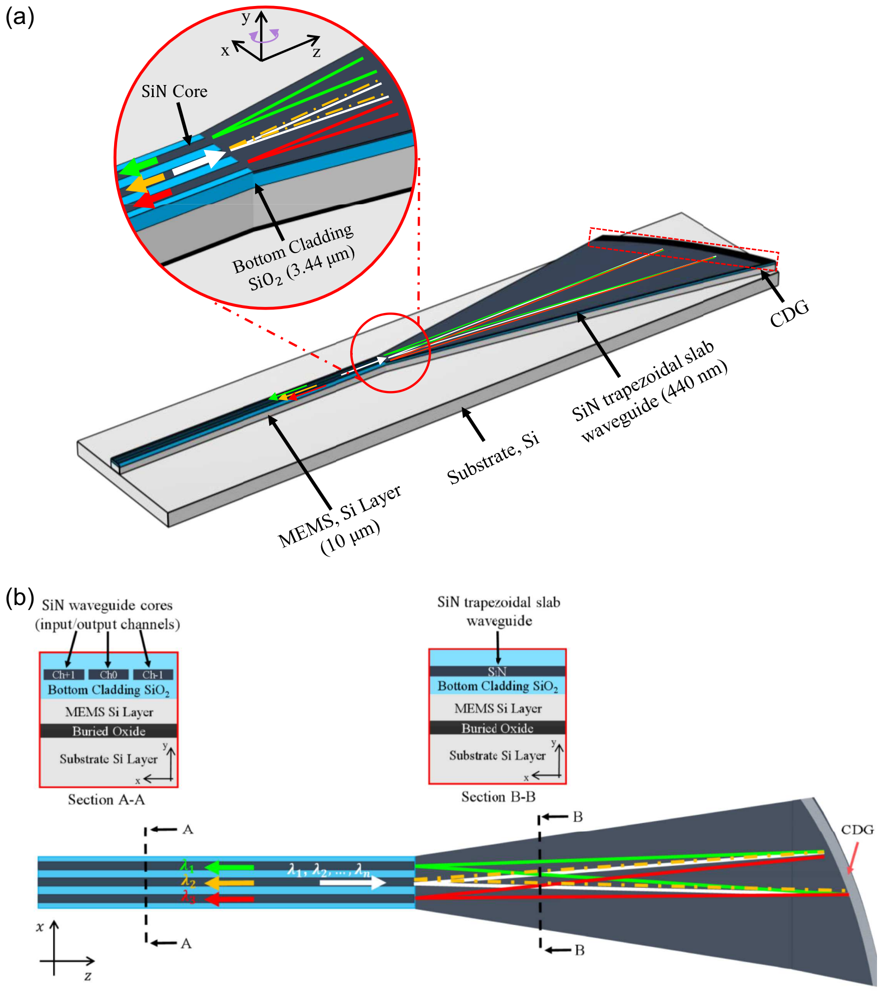

1.2.2. Mechanical platform and actuation strategy

Mechanical tuning is achieved by in-plane lateral displacement of the photonic structure using a MEMS-based silicon platform. Unlike gap-separated systems, all components are rigidly connected, forming a monolithic device. The resulting deformation alters the relative alignment between the waveguide entrances and the CDG, thereby modifying the routed wavelength.

To examine mechanical constraints, three configurations are defined by different boundary conditions, including support locations and load application points. These variations alter stiffness and deformation, with lateral forces shifting the wavelength routed to each output channel.

1.3. Scope of investigation

The scope of this study is limited to a modeling-driven analysis of the optomechanical response of monolithic MEMS-tunable WDM designs. The investigation examines how mechanical boundary conditions govern spectral response, with the objective of establishing quantitative design limits and performance trends across distinct configurations.

The analysis is based on Multiphysics simulations of deformation under applied forces, focusing on displacement and allowable travel range. These mechanical metrics are directly correlated with optical parameters, including wavelength tuning range, spectral linearity, and channel-spacing stability. Fabrication tolerances, process variability, packaging effects, and measurement uncertainties are not considered.

Fabrication-induced residual stress, thermomechanical coupling, and process variability are not explicitly included in the present analysis. Although these effects may influence absolute device performance and strain distribution, they are not expected to alter the fundamental optomechanical trends identified in this study. Their inclusion will be addressed in future experimental and modeling investigations.

In monolithic platforms, mechanical compliance and stress response are highly sensitive to boundary conditions, resulting in significant variation in required actuation forces across configurations. A simulation-driven approach is therefore adopted to identify feasible operating regimes, evaluate configuration-dependent performance trends, and guide future experimental implementation.

All materials, geometries, and actuation concepts are compatible with established silicon nitride photonic and MEMS processes. The results provide a quantitative design reference and a foundation for future experimental implementation.

The following sections describe the theoretical framework, modeling approach, and simulation methodology.

2. Methods and Modeling Approach

To investigate the optomechanical behavior of monolithic MEMS-tunable WDM systems under actuation, a two-dimensional (2D) finite-element method (FEM) framework is employed. This approach enables evaluation of force–displacement behavior and its impact on spectral response under fixed geometry and material properties.

The model assumes structural uniformity along the out-of-plane (y) direction, with vertical optical confinement incorporated through an effective index obtained from eigenmode analysis. This approach captures the dominant in-plane optomechanical interactions governing wavelength tuning, including lateral displacement and angular variation at the diffraction grating. Although fully three-dimensional effects, such as out-of-plane diffraction spreading and through-thickness stress gradients, are not explicitly resolved, the model accurately represents the relative tuning behavior and overall design trends. Full 3D analysis will be considered in future work to refine quantitative predictions.

The framework isolates mechanical effects by maintaining an identical optical layout comprising access waveguides, a trapezoidal slab, and a CDG while varying only boundary conditions and actuation locations (Figure 2). Three configurations are considered to ensure that variations in tuning behavior, linearity, and channel spacing arise solely from mechanical response.

Configuration I employs fixed–fixed boundary conditions with actuation at the slab entrance. Configuration II adopts a fixed–free condition, with the waveguide region clamped and actuation applied at the slab end. Configuration III introduces a fixed–anchored–free condition, adding two anchors at the slab entrance to modify stiffness, with actuation applied at the slab end.

In Configuration III, the anchored supports are implemented as compliant beam structures connecting the MEMS silicon layer to fixed sidewall regions. These beams act as flexural supports, enabling controlled rotation and limited translation under actuation. Their mechanical response is governed by beam geometry, with thickness and width determining stiffness and beam length controlling rotational compliance. Such suspended support structures are commonly realized in MEMS through selective release processes.

Figure 2

Three monolithic MEMS-tunable WDM configurations with identical optical layouts but different mechanical boundary conditions and actuation locations: (a) fixed–fixed, (b) fixed–free, and (c) fixed–anchored–free. Displacement direction, coordinate axes, and key geometric parameters are indicated

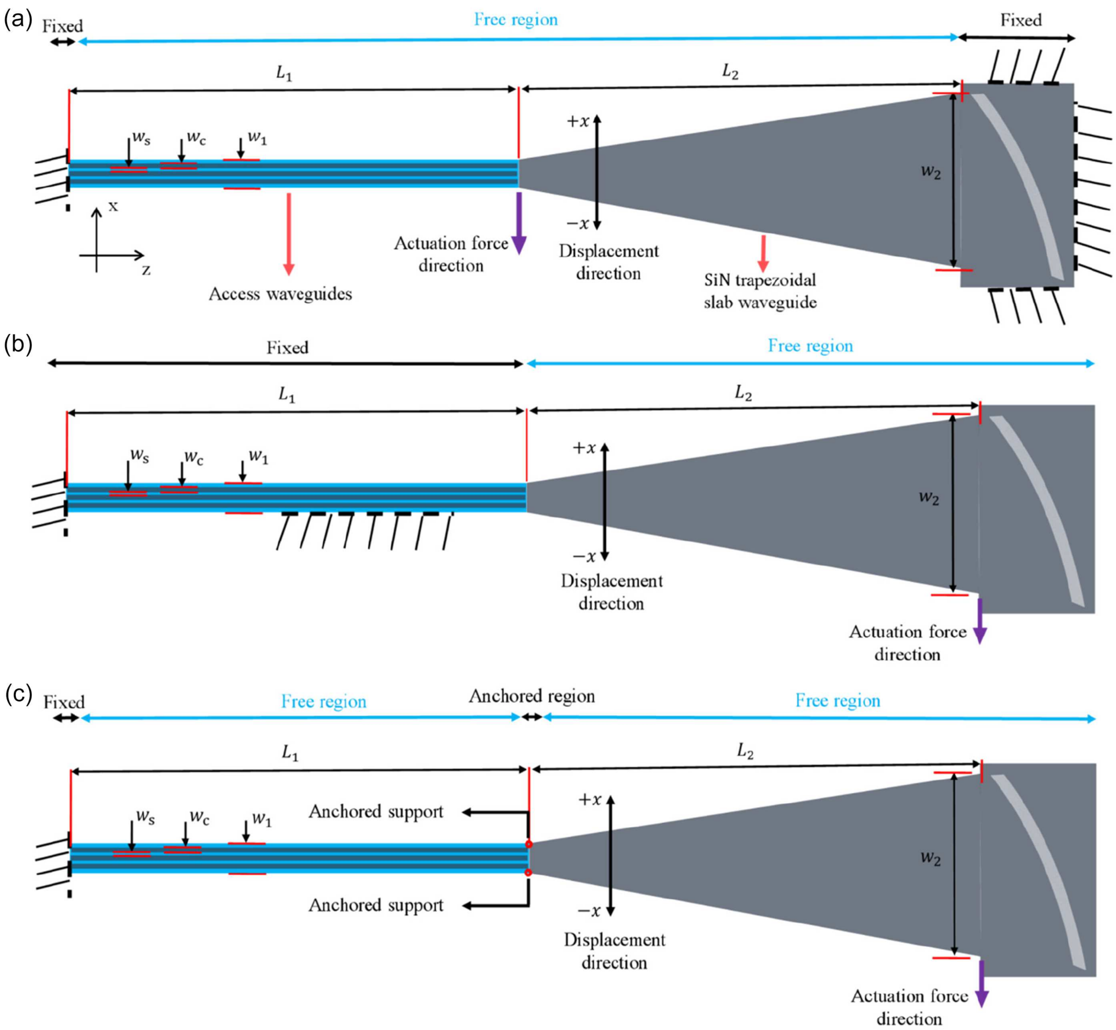

The mechanical response is computed using FEM of the monolithic SiN/SiO_2 platform, capturing elastic deformation under lateral actuation. Optical performance is evaluated through full-wave simulations to predict wavelength routing, spectral shift, insertion loss, and channel isolation. Coupling these models establishes a direct mapping between actuation force and spectral response.

This coupled optomechanical framework enables evaluation of mechanical compliance, tuning sensitivity, and spectral stability, which are difficult to assess experimentally in early design stages.

2.1. Mechanical modeling for predicting static behavior

The static mechanical behavior is modeled using FEM, where the structure is discretized to compute deformation under applied forces. The analysis focuses on the small-deflection regime relevant to MEMS operation, where actuator-induced displacements directly affect optical response. Accurate displacement prediction is therefore essential for evaluating wavelength tuning.

The multilayer SiN/SiO_2 structure can be treated as a sandwich system, with the SiN core embedded in SiO_2 cladding. The static response is obtained directly from FEM simulations using the defined geometry and material properties. The strain tensor is expressed in terms of displacement gradients as [27]:

$$\epsilon_{ij} = \frac{1}{2}\left(\frac{\delta u_i}{\delta x_j} + \frac{\delta u_j}{\delta x_i}\right) \tag{1}$$

where u_i are the displacement components and x_i denote spatial coordinates. In this formulation, the indices i, j correspond to the Cartesian coordinates of the device, where x denotes the lateral actuation direction and z is the optical propagation direction. Under lateral actuation, the deformation is primarily confined to the x–z plane, and the dominant strain components are ϵ_{xx} and ϵ_{xz}, which are directly obtained from the displacement field computed via FEM.

For an equivalent spring representation, the force–displacement relation can be approximated as:

$$F = k_{\mathrm{eff}}\Delta x \tag{2}$$

k_{eff} is extracted from the FEM response.

The device integrates three SiN access waveguides embedded in SiO_2 cladding. Light propagates into a trapezoidal slab, which directs it to a CDG in Littrow configuration (Figure 2).

The structure was modeled in COMSOL Multiphysics (Solid Mechanics) using the SiN/SiO_2 geometry and material properties listed in Tables 2 and 3. Boundary conditions and lateral actuation forces were applied as shown in Figure 2.

2.2 Modeling of the spectral response of the CDG

Wavelength separation is achieved using a CDG in Rowland geometry, which combines dispersion with focusing for compact multiplexing. The grating equation is given by [14]:

$$M\lambda = na(\sin\alpha + \sin\beta) \tag{3}$$

where M is the diffraction order, λ is the vacuum wavelength, a is the grating period, n is the effective refractive index, α is the incident angle, and β is the diffracted angle. To enhance efficiency, elliptical Bragg mirrors are incorporated, requiring the Bragg condition [14].

$$m\lambda = 2d\left[(1-f)n\cos\varphi + fn_2\sqrt{1-\left(\frac{n}{n_2}\right)^2\sin^2\varphi}\right] \tag{4}$$

where m is the Bragg order, d is the Bragg period, φ is the angle of incidence on the Bragg mirror, f is the filling fraction of the material with index of n_2, and n and n_2 are the effective refractive indices of the two materials.

The CDG follows Rowland geometry, with input and output waveguides placed on a circle of radius R_c, and the grating of radius $2R_c$, tangent to it. Light expands in the slab, reflects from an elliptical Bragg mirror, and is diffracted and refocused into wavelength-dependent channels (Figure 3 [17]). The mirror is formed using classical grating facets arranged as an elliptical Bragg reflector, extended to define the diffraction grating.

The geometric relations governing the Bragg mirror and diffraction structure are expressed as [14]:

$$\varphi = \frac{\alpha-\beta}{2},\ d = -a\sin\left(\frac{\alpha+\beta}{2}\right),\ \theta = \frac{-\alpha-\beta}{2} \tag{5}$$

Table 2
Geometry dimensions of the system

Symbol	Value (μm)	Description
w_c	3	The width of each SiN core
w_s	3	The separation width between the SiN cores
w_1	19	The width of the access waveguides stack
w_2	160	The end width of the trapezoidal slab before the CDG
L_1	414	The length of the access waveguides stack
L_2	410	The length of the trapezoidal slab before the CDG
t	7.32	Total mechanical stack thickness (SiO_2 + SiN + SiO_2)

Table 3
Mechanical properties of materials used in the simulations

Material	Young modulus (GPa)	Density (kg/m^3)	Poisson ratio
SiN	290	3100	0.24
SiO_2	72	2200	0.17

Figure 3
(a) Rowland-geometry schematic of the concave diffraction grating (CDG). (b) Elliptical Bragg mirror parameters, where grating stripes of index n_2 are placed along the ellipses within a background medium of index n

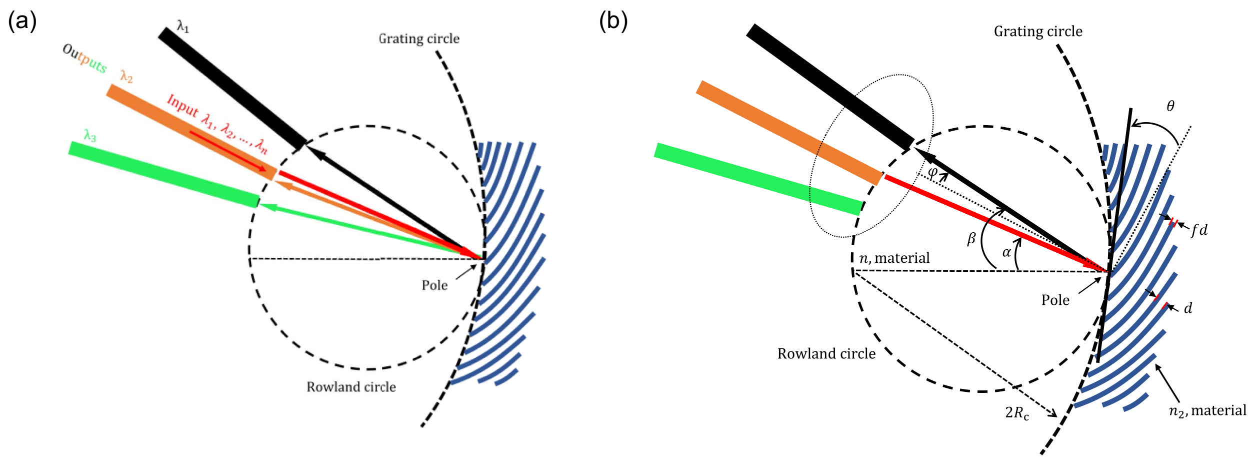

where θ represents the angle between the Bragg element and the grating front and φ denotes the angle of incidence on the Bragg mirror. Since the Bragg reflector is formed using two materials, the Bragg and diffraction orders are expected to be nearly equal in magnitude [14].

The diffraction geometry was designed using Rowland circle relations, with parameters determined by the target wavelength (1538, 1550, and 1562 nm), channel spacing (12 nm), and the refractive indices of SiN and SiO_2 (Table 4).

To analytically predict the optical response of the device, light propagation in the slab region was modeled using the two-dimensional Rayleigh–Sommerfeld diffraction integral (Eq. 6). This formulation accounts for both diffraction and focusing effects and enables calculation of the complex optical field distribution within the slab region [17, 28]:

$$U_2(x_2, z_2) = i\pi n \frac{z_2}{\lambda} \int_{-\infty}^{+\infty} \mathrm{U}_1(x_1, 0) \frac{1}{r} H_1^{(1)}\left(\frac{2\pi n r}{\lambda}\right) dx_1 \quad (6)$$

where U_2 represents the optical field at the point (x_2, z_2), U_1 denotes the source field at $(x_1, 0)$, $r = \sqrt{(x_2 - x_1)^2 + z_2^2}$ is the

Table 4
Elliptical Bragg grating and access waveguide parameters

Symbol	Value	Description
λ_c	1.55 μm	Central operation wavelength
α	–45°	Incident angle on the diffraction grating
β	–42.7°	Diffracted angle
n_{eff}	1.7874	The effective index for the slab waveguide according to the core thickness (n_{eff} = n)
t_{SiN}	0.440 μm	SiN core thickness
n_{SiN}	2.0208	SiN index at λ_c
n_{SiO_2}	1.444	SiO_2 index at λ_c, $n_2 = n_{SiO_2}$
M	–2	Diffraction order
a	1.286 μm	Diffraction grating period
d	0.891 μm	Bragg period
f	0.14	Bragg filling factor ratio of the n_{SiO_2} width to the d
θ	43.85°	Angle between Bragg element and the grating front
ψ	–1.15°	Angle of incidence on the Bragg mirror
n_b	20	Number of Bragg mirror periods
$2R_c$	500 μm	Rowland circle diameter
w_{core}	3 μm	Waveguide width
w_1	19 μm	Entrance width of the trapezoidal slab
w_2	160 μm	End width of the trapezoidal slab
L_1	414 μm	Length of the access waveguide and SOI cantilever
L_2	410 μm	Length of the trapezoidal slab
$\Delta\lambda$	24 nm	Spectral wavelength distance between the first and last channel

spatial distance between the observation point and source, n is the effective refractive index, and $H_1{}^{(1)}$ is the first kind and first order of the Hankel function. This formulation provides a rigorous analytical framework for modeling diffraction and focusing in CDG-based devices.

To further validate the analytical predictions, full-wave electromagnetic simulations were performed using the FEM in COMSOL Multiphysics. The Electromagnetic Waves, Frequency Domain (EWFD) module was employed to model light propagation through the SiN access waveguides, the trapezoidal slab region, and the CDG. Effective refractive indices obtained from 2D eigenmode analysis were used to account for vertical confinement of the optical modes.

To suppress spurious reflections at the simulation boundaries, perfectly matched layers (PMLs) were introduced. Local mesh refinement using a tetrahedral discretization was applied in regions exhibiting strong field gradients to ensure numerical accuracy. Channel transmission was calculated by integrating the time-averaged Poynting vector at the output waveguides.

In the frequency domain, the electric field EEE satisfies the vector wave equation derived from Maxwell's curl–curl formulation:

$$\nabla \times \mu_r^{-1}(\nabla \times \boldsymbol{E}) - k_0^2\left(\varepsilon_r - \frac{j\sigma}{\omega\varepsilon_0}\right)\boldsymbol{E} = 0 \qquad (7)$$

Assuming a guided wave propagating along the z-axis, the electric field can be expressed as

$$E(\mathrm{x}, \mathrm{y}, \mathrm{z}) = \tilde{E}(\mathrm{x}, \mathrm{y})\, e^{-j\beta z} \qquad (8)$$

where $k_0 = \frac{2\pi}{\lambda}$ is the free-space wavenumber, $\beta = k_z$ is the propagation constant, and $\tilde{E}(x, y)$ represents the transverse mode distribution. The parameters ε_r and μ_r denote the relative permittivity and permeability distributions, and σ is the electrical conductivity [29]. Applying the Galerkin method with curl-conforming Nédélec finite elements reduces the governing equations to a sparse algebraic system:

$$\left(K - k_0^2 M + B\right)\boldsymbol{e} = \boldsymbol{f} \qquad (9)$$

where K is the curl-curl stiffness matrix, M is the dielectric mass matrix, B represents boundary contribution, and $\boldsymbol{f}$ the excitation vector [29]. Solving this system provides the expansion coefficients $\boldsymbol{e}$ of the electric field.

The mesh resolution was selected relative to the optical wavelength, with a minimum element size of approximately $\lambda/20$ in regions of strong field variation. Additional local refinement was applied near waveguide interfaces and the diffraction grating. Mesh convergence was verified through the stability of transmission spectra and peak wavelength positions under further refinement, with negligible variation observed, confirming sufficient numerical accuracy for the present analysis.

Together, the analytical diffraction model and FEM-based electromagnetic simulations provide complementary approaches for evaluating the spectral behavior of the CDG. The analytical model enables rapid optimization of the diffraction geometry, while the FEM simulations provide rigorous full-wave verification of the optical response of the integrated photonic microsystem.

3. Results and Discussion

Device performance was evaluated using analytical modeling and finite-element simulations in COMSOL Multiphysics. Mechanical analysis was used to determine structural deflection and effective stiffness under actuation, while optical simulations verified wavelength routing through the CDG.

The results are presented in three parts: (i) mechanical response under actuation, focusing on deflection and stiffness; (ii) spectral response without actuation, including CDG diffraction and channel spacing across the C-band; and (iii) coupled optomechanical behavior, demonstrating wavelength tuning across the three configurations. Together, these results highlight the role of mechanical compliance in shaping WDM spectral performance.

To enable direct comparison between configurations, actuation was modeled using an equivalent applied force independent of a specific actuator implementation.

3.1. Mechanical response of the monolithic WDM systems under actuation

The mechanical analysis defines actuation limits and displacement stability required for efficient optical coupling. These results inform optical simulations of the CDG, where controlled lateral displacement determines the wavelength-tuning range. Together, they enable system-level evaluation of monolithic configurations.

The boundary conditions for the three configurations are illustrated in Figure 4: Configuration I (Figure 4(a)) is fixed at both ends; Configuration II (Figure 4(b)) is fixed at the access waveguide region; and Configuration III (Figure 4(c)) is fixed at one end with additional anchors at the slab entrance, corresponding to the junction between the access waveguides and slab.

A static structural analysis was performed to evaluate elastic displacement under lateral actuation and assess suitability for MEMS–photonic integration. To extract the effective spring constant, the point of force application was prescribed a target displacement of ±5 μm, and the corresponding actuation force was recorded.

The simulations show distinct behaviors across configurations. Configuration I exhibits asymmetric bending before the slab entrance, indicating reduced displacement stability. Configurations II–III require significantly lower actuation forces but show nonuniform lateral motion of the CDG due to a z-direction offset between the first and last grating elements.

The force–displacement results further highlight these differences. Configuration I requires 43.16 mN for a ±5 μm displacement, corresponding to a stiffness of ~8632 N/m. In contrast, Configurations II–III show much lower stiffness (330 N/m and 260.6 N/m, respectively) but exhibit nonuniform CDG displacement that may degrade optical performance.

Overall, these results establish the mechanical feasibility and limits of the monolithic platform for dynamic wavelength tuning in a three-channel WDM system. Building on this, the next section evaluates the spectral response under zero actuation, providing a baseline for assessing actuation-induced tuning.

3.2. Spectral response of the monolithic WDM system under no actuation

After verifying mechanical stability, the optical performance of the monolithic CDG is evaluated using two complementary approaches: (i) an analytical model based on Rayleigh–Sommerfeld diffraction with a 2D slab approximation and (ii) full-wave finite-element simulations in COMSOL Multiphysics. Together, they provide physical insight and numerical verification of wavelength

Figure 4

Static structural displacement profiles for the three configurations. (a) Configuration I exhibits high stiffness, requiring larger actuation forces and localized bending near the trapezoidal slab entrance. (b) and (c) Configurations II and III require lower actuation forces but exhibit nonuniform CDG displacement due to positional offset, with Configuration III additionally introducing bending in the access waveguide region

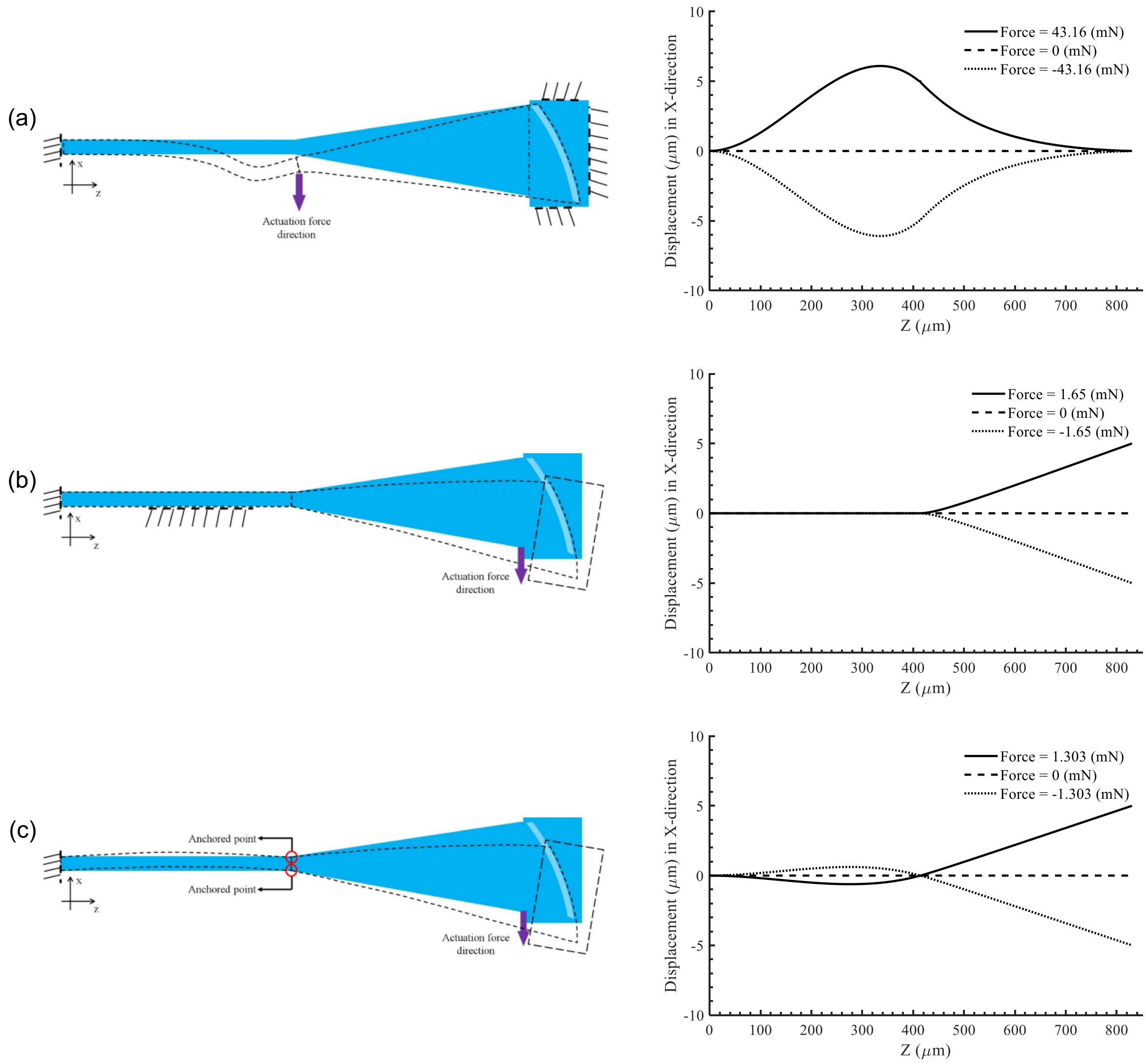

routing, insertion loss, channel isolation, and overall spectral performance.

The analytical model applies the two-dimensional Rayleigh–Sommerfeld integral to compute the optical field at the output plane, treating the CDG as the radiating source. This formulation captures diffraction and focusing in Rowland geometry and enables rapid evaluation of channel response and power distribution.

For the unactuated device, the model predicts three channels at 1538 nm, 1550 nm, and 1562 nm, with 12 nm spacing. Peak efficiencies reach ~0.875–0.892 with insertion loss below 0.6 dB. Adjacent-channel isolation exceeds 32 dB (worst-case crosstalk of ~−30 dB), and each channel has a ~5.49-nm 3-dB bandwidth.

Complementary frequency-domain FEM simulations were performed using the EWFD module in COMSOL. Effective-index mapping and parameters from Table 4 were used. Light was launched into the central waveguide (Ch0) with out-of-plane polarization, and the wavelength was swept from 1520 to 1580 nm in 0.5 nm steps. Adaptive meshing, scattering boundary conditions, and time-averaged Poynting vector evaluation ensured accurate power computation.

Transmitted power was obtained by integrating the Poynting flux at the outputs and normalizing to the input. Figure 5 compares analytical (Figures 5(a)–(b)) and FEM (Figures 5(c)–(d)) results on linear and dB scales. The domain was enclosed by PMLs, suppressing spurious reflections and sidelobe artifacts [17].

Table 5 summarizes the performance metrics. Both approaches show good agreement in channel wavelengths, bandwidths, and insertion loss, with high efficiencies and total loss below 1 dB.

The higher isolation predicted by the analytical model arises from idealized assumptions of Gaussian excitation, 2D diffraction, and perfect geometry, while neglecting scattering, higher-order effects, mode mismatch, and boundary effects. In contrast, FEM simulations incorporate finite-aperture effects and these non-idealities, yielding a more realistic, conservative, and fabrication-relevant estimate.

Figure 5
Transmission characteristics of the three output channels from analytical modeling (a, b) and FEM simulations (c, d). Analytical results: (a) normalized power spectra of Ch-1, Ch0, and Ch+1 and (b) corresponding dB-scale responses showing channel isolation and crosstalk. FEM results: (c) normalized spectra and (d) dB-scale responses, obtained by launching out-of-plane light into Ch0 with a wavelength sweep from 1520 to 1580 nm

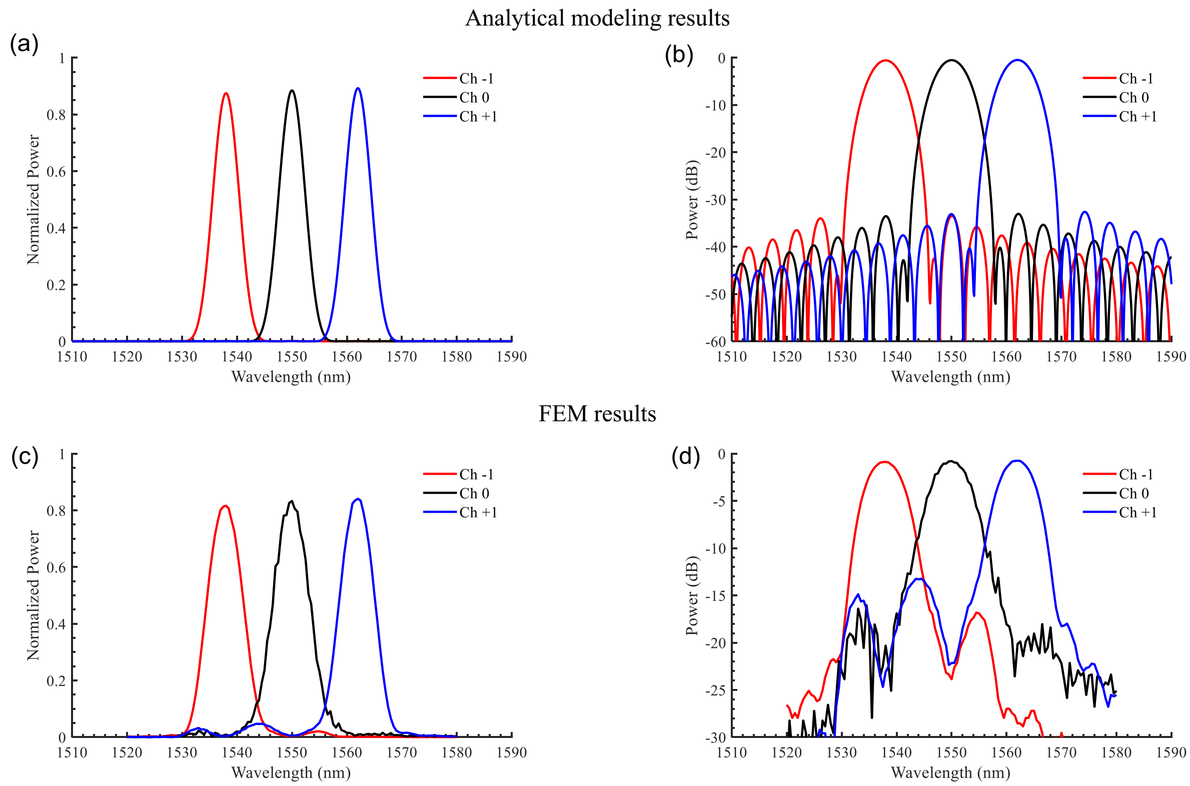

Table 5
Summary of the detailed specification of the channel for the analytical method and FEM

Definition	Method	Ch-1	Ch0	Ch+1
Wavelength (nm)	Analytical	1538	1550	1562
	FEM	1538	1550	1562
Power efficiency at peak	Analytical	0.875	0.884	0.892
	FEM	0.816	0.832	0.840
Insertion loss (dB)	Analytical	0.58	0.54	0.49
	FEM	0.88	0.79	0.75
3 dB bandwidth (nm)	Analytical	5.494	5.495	5.497
	FEM	7	7	6.5
Adjacent-channel isolation (dB)	Analytical	32.9	32.5	32.6
	FEM	~19.5	~21.5	~19.5
Total crosstalk (dB)	Analytical	32.7	29.7	32.2
	FEM	~19.5	~21.5	~19.5

Despite these differences, both approaches confirm robust wavelength routing with low insertion loss and clear channel separation. Spectral fluctuations in the central channel (Ch0) in the FEM results arise from its dual role as both input and output, increasing sensitivity to residual interference.

Building on the zero-actuation baseline, the following subsection examines how mechanical actuation modifies the optical response, with a focus on optomechanical wavelength tuning in the monolithic WDM system.

3.3. Optomechanical response under actuation

Mechanical actuation was used to investigate the spectral tunability of the monolithic WDM architectures under identical lateral forces of −4.316, −2.158, no force (corresponding to the unactuated state), +2.158, and +4.316 mN. Light was injected through the central waveguide, which also served as the central output channel (Ch0), while optical power was monitored at Ch−1, Ch0, and Ch+1. The complete optical system was modeled using frequency-domain electromagnetic simulations in COMSOL Multiphysics. All simulations were performed under identical optical and numerical conditions, with local mesh refinement applied in regions of strong field gradients to ensure accurate evaluation of the Poynting vector.

Mechanical deformation modifies the relative orientation between the input waveguides and the CDG, thereby tuning the wavelength routed to each output channel. This response is governed by the effective optical angle $\delta\theta = \beta - \alpha$, where α and β denote the rotations of the waveguide entrance and grating, respectively. Because the resulting lateral displacement depends on the mechanical boundary conditions, identical actuation forces produce distinct spectral responses across the three configurations.

Configuration I exhibits the stiffest mechanical response, in which tuning is achieved by translating and slightly rotating the waveguide entrances relative to the fixed CDG, while both elements remain aligned along the Rowland circle. The resulting spectral response yields a tuning range of approximately 4 nm per channel under double-sided actuation.

In Configuration II, the bending of the trapezoidal slab induces translation and rotation of the CDG, such that tuning becomes dominated by grating rotation rather than waveguide motion. This leads to enhanced spectral sensitivity, yielding a substantially larger tuning range of ~8.5–9 nm per channel, more than twice that of Configuration I, albeit with increased spectral nonuniformity arising from the reduced structural stiffness. The broader tuning response reflects the reduced structural stiffness and stronger CDG rotation under actuation.

Configuration III permits controlled rotation while suppressing excessive deformation through anchored slab entrances. Although mechanically more compliant, the anchors stabilize the grating motion and produce a spectral response comparable to that of Configuration II, with a tuning range of ~8.5–9 nm per channel. The larger rotational motion of the CDG under actuation, accompanied by longitudinal displacement, indicates that greater mechanical deformation is required to achieve equivalent wavelength shifts, highlighting the trade-off between mechanical compliance and spectral sensitivity.

Figure 6 shows the simulated field distributions under representative actuation forces, confirming wavelength routing consistent with Rowland geometry, in which Ch−1 and Ch+1 collect shorter and longer wavelengths, respectively, relative to Ch0 (the field distributions of the remaining channels are presented in the Supplementary Materials, Figure S1, Figure S2, and Figure S3). The corresponding normalized spectra in Figure 7 demonstrate that mechanical boundary conditions strongly govern tuning sensitivity, linearity, and spectral uniformity.

3.4. Linearity and tuning performance

The wavelength-tuning behavior of the three monolithic configurations is primarily governed by structural stiffness and the resulting angular variation at the CDG, which directly influences wavelength routing. Figure 8 presents the wavelength shift under applied force, while Table 6 summarizes the key mechanical and optical performance parameters, including stiffness, effective CDG rotation sensitivity, channel spacing, and wavelength–force sensitivity.

Configuration I exhibits the highest stiffness (8632 N/m), resulting in limited CDG rotation and a wavelength sensitivity of 0.463 nm/mN. Consequently, the tuning range is restricted to approximately 4 nm per channel under ±4.316 mN. However, this configuration demonstrates excellent linearity, constant channel spacing (~12 nm), and minimal displacement, indicating stable and predictable wavelength routing dominated by translational motion.

Configuration II reduces the stiffness to 330 N/m, increasing the rotational sensitivity and wavelength-tuning sensitivity to approximately 1.027 nm/mN. As a result, the tuning range increases by more than a factor of two relative to Configuration I under identical actuation conditions. By comparison, the enhanced rotational deformation also introduces slight spectral nonlinearity and moderate channel-spacing variation (11.5–12.5 nm). These effects highlight the trade-off between tuning sensitivity and spectral uniformity.

Configuration III has the lowest stiffness (260.6 N/m) and exhibits tuning sensitivity comparable to that of Configuration II.

Figure 6

Simulated optical field distributions of channel Ch0 for the three device configurations: (a) Configuration I, (b) Configuration II, and (c) Configuration III, under actuation forces of −4.316 mN and +4.316 mN. Mechanical deformation is exaggerated for clarity, with displacement scaling factors of 50, 2, and 10 for Configurations I–III, respectively. Simulated optical field distributions for the remaining channels are provided in the Supplementary Document (Figures S1–S3)

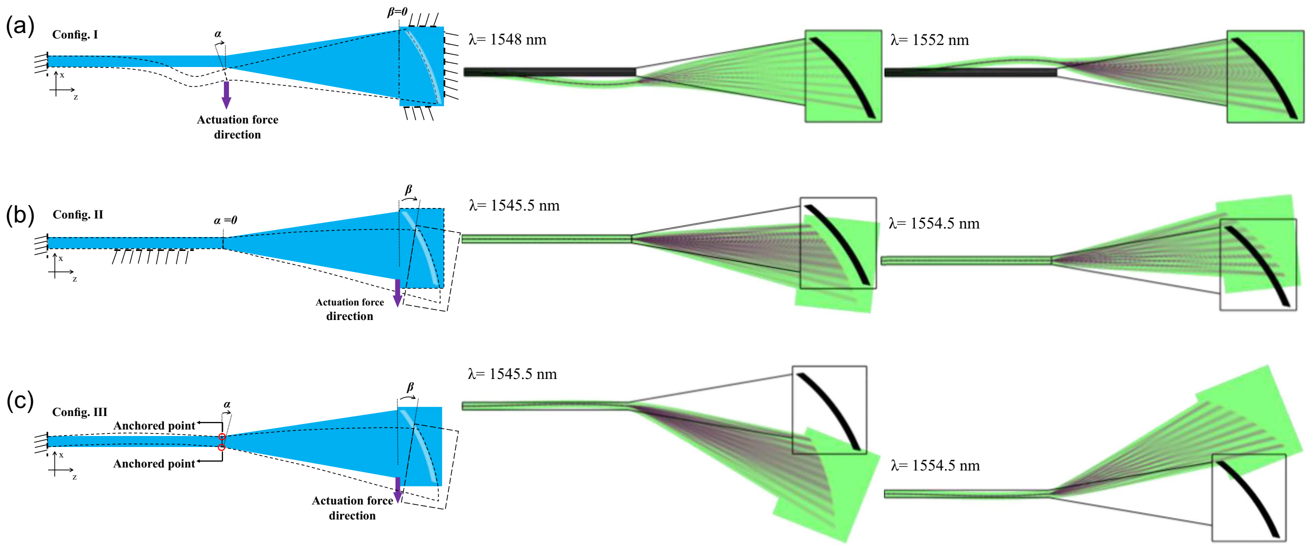

Figure 7
Normalized power spectra of channels Ch−1, Ch0, and Ch+1 for Configuration I (a–c), Configuration II (d–f), and Configuration III (g–i), respectively, under actuation forces ranging from −4.316 mN to +4.316 mN

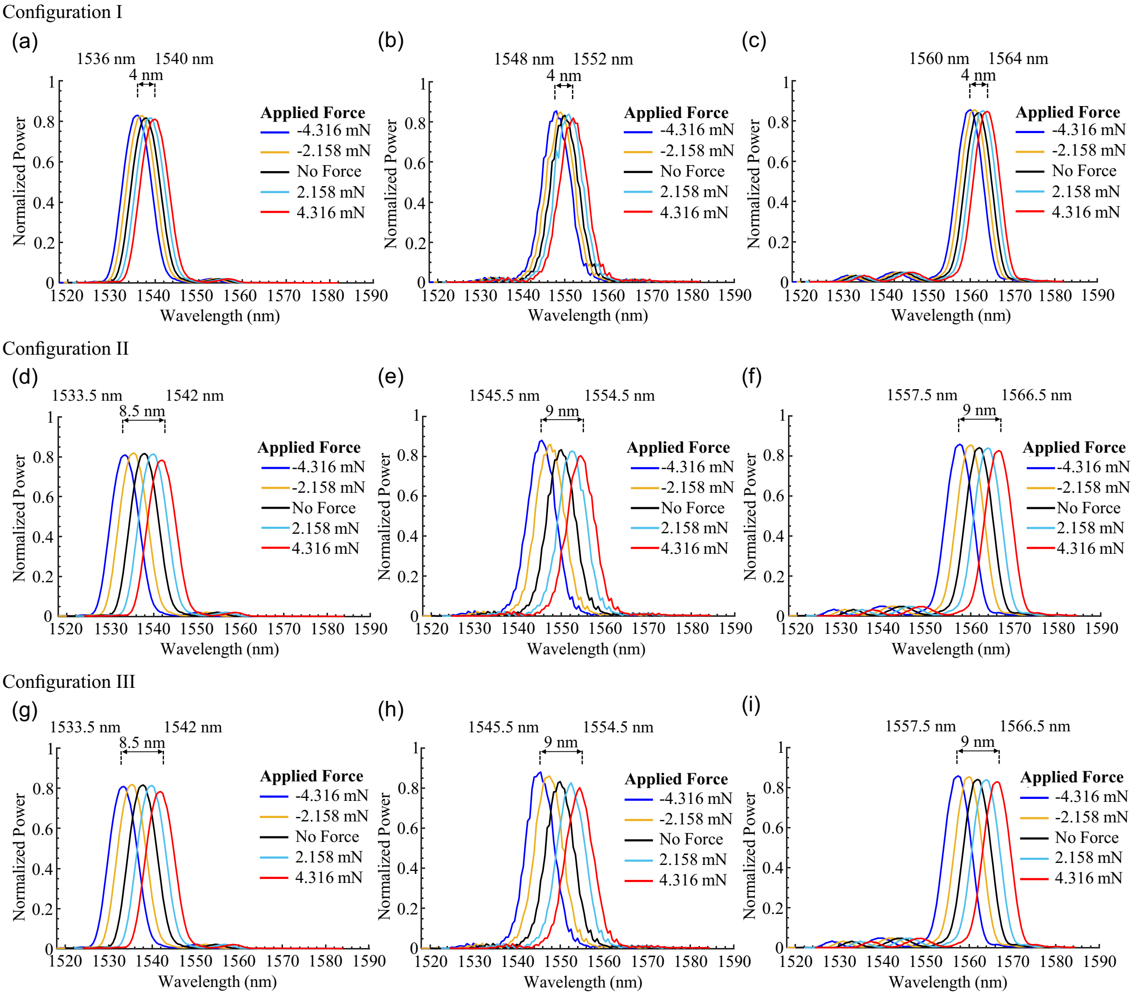

Figure 8
Relationship between applied force and wavelength shift for each output channel: (a) Configuration I, (b) Configuration II, and (c) Configuration III

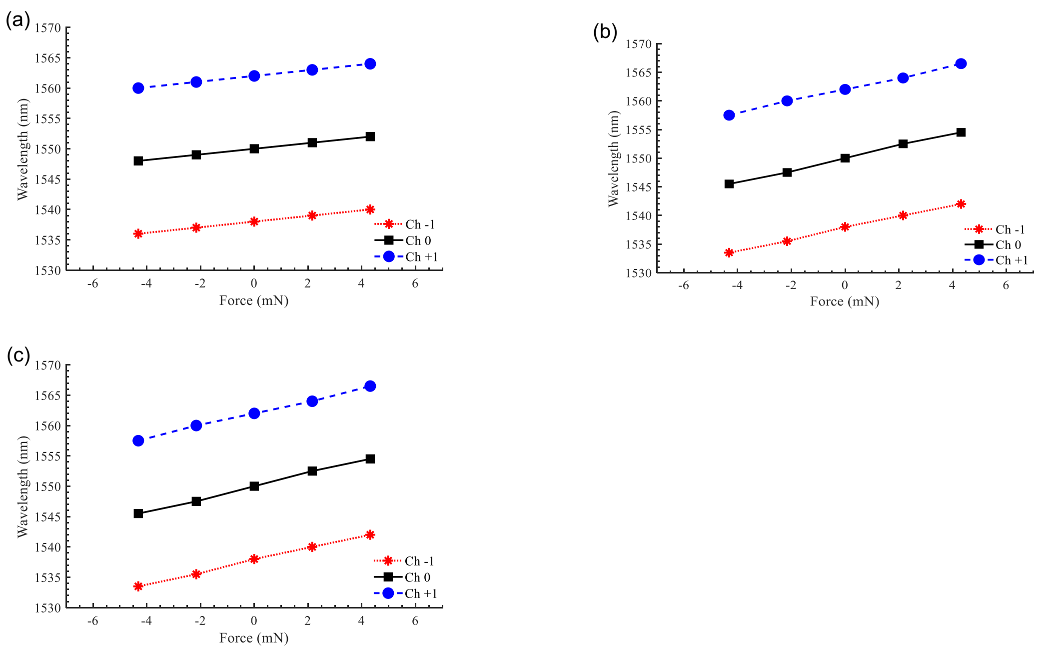

Table 6
Comparative summary of the three monolithic configurations

Configuration	Configuration I	Configuration II	Configuration III
Stiffness, k (N/m)	8632	330	260.6
Effective CDG rotation sensitivity, $\Delta\theta/\Delta F$ (°/mN)	0.018	0.42	0.47
Channel-spacing range under actuation, $\Delta\lambda_{ch}$ (nm)	12	11.5–12.5	11.5–12.5
Wavelength sensitivity to force, $d\lambda/dF$ (nm/mN)	0.463	~1.027	~1.027

The combined rotational and longitudinal deformation restores near-linear behavior; however, a larger displacement is required to achieve the same wavelength shift.

Overall, Configuration I provides the highest linearity and spectral uniformity, whereas Configurations II and III achieve substantially larger tuning ranges through enhanced grating rotation at the expense of increased deformation and reduced channel-spacing uniformity. These findings establish the interplay between stiffness, displacement, and optical alignment as a key design principle for mechanically tunable WDM systems under practical actuation constraints [24].

These differences in stiffness and displacement requirements also have direct implications for practical MEMS actuator implementation, which are examined in the following section.

3.5. Mechanical design trade-offs

The optomechanical results presented in the previous section demonstrate that the three configurations exhibit significantly different stiffness and wavelength-tuning sensitivities under identical actuation forces. To relate these behaviors to practical MEMS implementation constraints, the required actuation forces and displacement demands are evaluated using an electrostatic comb-drive actuator model.

Although Configurations II and III require lower actuation force than Configuration I, they require larger mechanical displacement to achieve comparable wavelength tuning, resulting in a trade-off among actuation force, actuator footprint, stability, and fabrication complexity.

The lateral electrostatic force is given by [30]:

$$F_{ele} = \left(\frac{n\varepsilon_0 t V^2}{\mathrm{d}}\right) \tag{10}$$

where n is the number of comb fingers, t is the finger thickness, d is the finger gap, V is the applied voltage, and ε_0 is the air permittivity. Prior to pull-in instability, the electrostatic force is balanced by the restoring mechanical force:

$$F_{mech} = k_x x \tag{11}$$

where k_x is the effective stiffness and x is the lateral displacement. Based on Eq. (10), the number of comb fingers required to achieve a target displacement can be estimated. Stable operation requires the actuator gap to exceed approximately three times the maximum displacement to avoid pull-in instability, lateral misalignment, and comb-finger contact, thereby defining the required finger-engagement area for a given wavelength shift.

The actuator area can be approximated as:

$$Area = n \times A_1 \tag{12}$$

where A_1 is the area of a single engaged comb, as illustrated in Figure 9(a). Under equal voltage and footprint conditions, Configuration I exhibits the highest force density $\left(\sigma = \frac{Force}{Footprint}\right)$ because of its larger stiffness, whereas Configurations II and III achieve larger deformation at lower force. In contrast, their increased rotation and travel requirements introduce additional fabrication and reliability challenges. Precise control of both translation and rotation is required to avoid comb-finger pull-in. In addition, the larger displacement required for a given wavelength shift may increase mechanical stress and affect long-term reliability.

Mechanical deformation primarily shifts the operating wavelength while preserving the overall spectral response. Although stress-induced refractive-index variations and geometric deformation may introduce minor changes in insertion loss and crosstalk,

Figure 9
(a) Electrostatic comb-drive actuator schematic showing the single-finger comb and the corresponding area, A1, (b) force density versus actuator travel for the three configurations with a footprint of 4 × 4 mm², and (c) wavelength-tuning span versus actuator travel for a maximum displacement of 5 µm

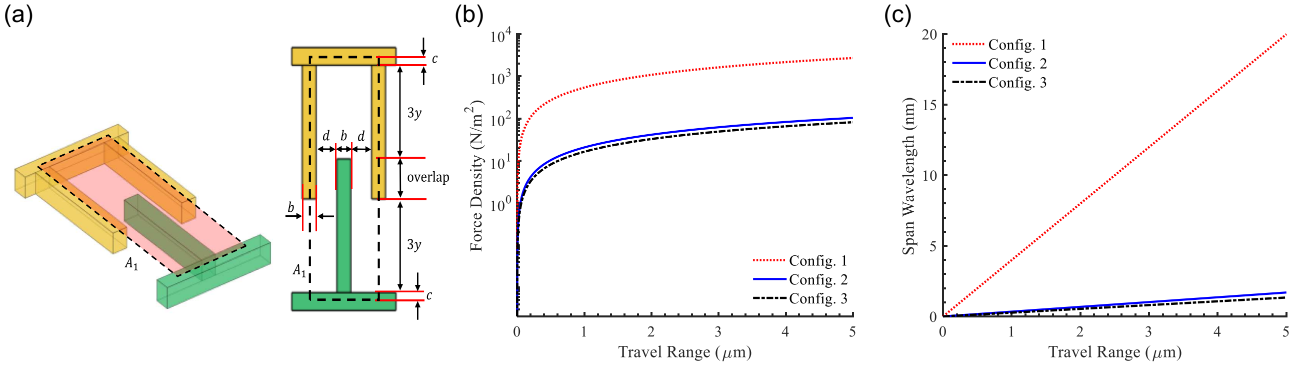

these effects remain secondary within the considered operating range.

To compare actuator requirements, a rectangular comb-drive actuator with a 4 × 4 mm² footprint and a maximum travel of 5 µm is assumed, using d = 2 µm, t = 10 µm, b = 2 µm, c = 5 µm, and an overlap length of 2 µm. Figure 9(b) shows that Configuration I requires the highest force density due to its high stiffness, whereas Configurations II and III require significantly lower force densities. Figure 9(c) shows that Configuration I achieves the largest wavelength-tuning span (∼20 nm), whereas Configuration III requires the lowest force but offers the smallest tuning range. Configuration II offers a balanced trade-off between tuning range and actuator demand.

The present analysis is limited to electrostatic comb-drive actuators; alternative approaches such as electrothermal or piezoelectric actuation may provide improved performance for Configurations II and III.

Overall, the results demonstrate that mechanical compliance strongly governs the trade-off between tuning sensitivity and structural stability. Configuration I prioritizes robustness, spectral uniformity, and tuning range, whereas Configurations II and III improve force sensitivity at the expense of larger displacement and reduced mechanical stability. From an integration perspective, lower stiffness reduces actuation force and power consumption, enabling more compact and potentially faster MEMS platforms. Therefore, co-optimization of CDG geometry, mechanical constraints, and actuator architecture is essential for achieving a compact, energy-efficient, and mechanically stable platform.

The extracted stiffness values further suggest that the fundamental mechanical resonance lies in the kHz-to-low-MHz range, indicating the potential for moderate-speed optical switching operation. A detailed transient and dynamic analysis, including switching time, resonance behavior, and damping effects, is beyond the scope of the present work and will be addressed in future studies.

3.6. Fabrication feasibility and practical considerations

The practical implementation of the proposed architectures is considered in the following section. The proposed system is compatible with established CMOS silicon nitride (SiN) photonic and MEMS fabrication processes [8]. The device can be implemented on an SOI platform, where the silicon device layer serves as the MEMS structural layer and the buried oxide functions as both the sacrificial layer and optical cladding.

A representative fabrication flow for Configuration I is illustrated in Figure 10. The device can be implemented on an SOI platform using standard MEMS and silicon nitride photonic fabrication processes, including thin-film deposition, lithographic patterning, anisotropic etching, and sacrificial release techniques. The Si device layer defines the movable MEMS platform and comb-drive actuators, while the SiN layer forms the waveguides, trapezoidal slab, and CDG embedded within SiO_2 cladding layers. Selective release of the sacrificial oxide creates the suspended MEMS structure required for mechanical actuation.

During micromachining, suspended regions are formed through the selective removal of the sacrificial oxide layer using DRIE, resulting in an air-suspended MEMS structure. The compliant support beams remain anchored to fixed substrate regions,

Figure 10

Fabrication flow of the suspended SiN photonic device integrated with MEMS actuation. (a) Formation of the buried oxide layer on the silicon substrate. (b) Patterning of the polysilicon structural layer defining the MEMS platform. (c) Formation of metal pads for electrical interfacing. (d) Deposition of the lower SiO_2 cladding. (e) Patterning of the SiN optical layer, including the waveguides and concave diffraction grating (not to scale). (f) Deposition of the upper SiO_2 cladding. (g) Application of a protective layer prior to release. (h) Selective removal of the sacrificial oxide layer to release the suspended structure. (i) Final released device comprising the fully clad SiN photonic stack integrated on a movable polysilicon MEMS platform

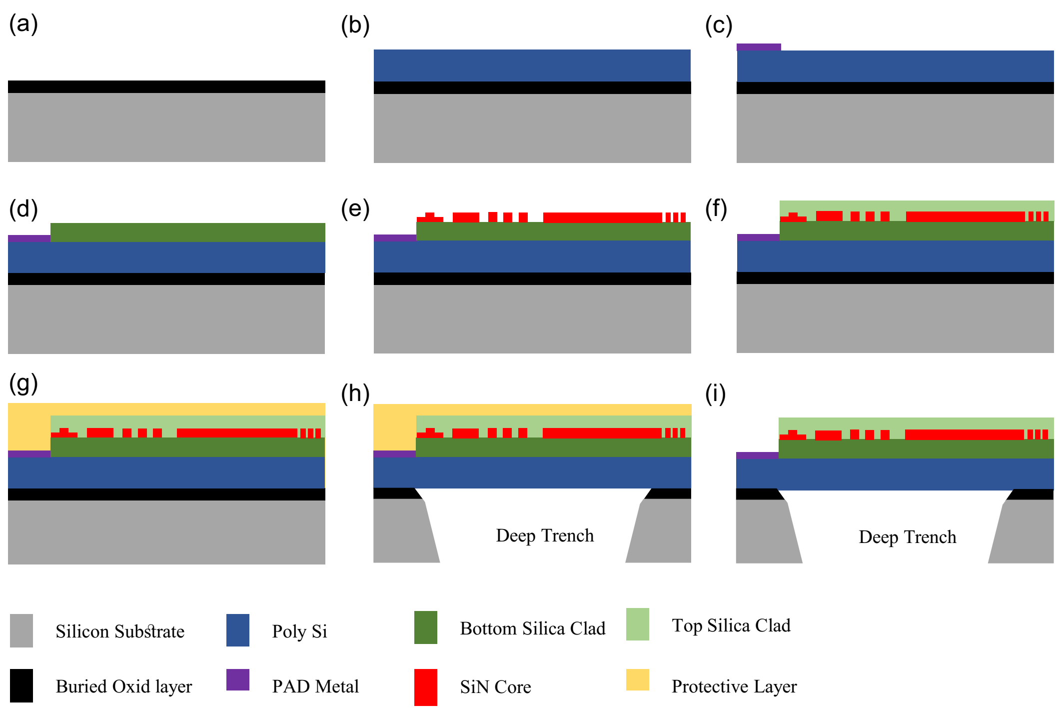

enabling controlled mechanical deformation under electrostatic actuation while preserving structural stability.

Key fabrication challenges include maintaining high lithographic precision in the CDG, as period variations directly affect spectral response and channel isolation, as well as accurately controlling the release air gap. Nevertheless, lateral misalignment mainly produces predictable spectral shifts rather than abrupt degradation, while the monolithic architecture inherently preserves vertical alignment. Although fabrication tolerances, residual stress, release-induced deformation, and long-term reliability effects such as stiction, fatigue, and pull-in instability are not explicitly modeled, the proposed geometry remains within practical limits of current MEMS and integrated photonic technologies, supporting the feasibility of future experimental validation and system-level optimization.

4. Conclusion

This study presents a systematic mechanical–spectral comparison of three monolithic MEMS-tunable Littrow WDM configurations integrating silicon nitride waveguides with a CDG. By isolating the mechanical boundary conditions while maintaining an identical optical layout, the coupling among structural stiffness, angular variation at the CDG, and spectral tuning behavior is quantitatively established.

The results demonstrate that mechanical boundary conditions dictate wavelength-tuning performance. The fixed–fixed configuration provides superior linearity, nearly constant channel spacing, and minimal displacement but requires higher actuation force and exhibits reduced tuning sensitivity per unit force, despite enabling the largest wavelength span when actuator travel is considered. The fixed–free configuration offers a balanced compromise, reducing stiffness and nearly doubling tuning sensitivity while maintaining acceptable spectral uniformity. The fixed–anchored–free configuration increases sensitivity relative to Configuration I through rotation-dominated deformation while limiting compliance, partially restoring near-linear behavior, and yielding performance comparable to Configuration II.

Across all configurations, a clear trade-off emerges between tuning sensitivity and structural stability. Higher compliance improves tuning efficiency at the expense of structural rigidity. These results demonstrate that optimal monolithic MEMS–photonic integration requires co-optimization of boundary conditions, CDG geometry, and actuator design.

Quantitatively linking structural stiffness, angular variation, and spectral response, this work provides a predictive framework for designing compact, low-loss, energy-efficient, and mechanically stable monolithic WDM systems. The results serve as a reference for future fabrication and experimental validation of MEMS-integrated photonic multiplexers. Future work will focus on experimental realization and dynamic characterization of the proposed architectures.

Acknowledgment

The authors acknowledge CMC Microsystems and the Digital Research Alliance of Canada for providing the design and computational resources used in this work.

Funding Support

This work was supported by the Natural Sciences and Engineering Research Council of Canada (NSERC) through the Discovery Grant, Strategic Grant, and Concordia University Research Chair Program awarded to Prof. M. Packirisamy.

Ethical Statement

This study does not contain any studies with human or animal subjects performed by any of the authors.

Conflicts of Interest

The authors declare that they have no conflicts of interest to this work.

Data Availability Statement

Data are available from the corresponding author upon reasonable request.

Author Contribution Statement

Mehdi Kharazmi: Conceptualization, Methodology, Software, Validation, Formal analysis, Investigation, Data curation, Writing – original draft, Visualization. **Pierre Pottier:** Software, Validation, Investigation, Resources, Data curation. **Jayan Ozhikandathil:** Software, Validation, Investigation, Data curation, Writing – review & editing, Supervision. **Muthukumaran Packirisamy:** Conceptualization, Software, Validation, Investigation, Resources, Data curation, Writing – review & editing, Supervision, Project administration, Funding acquisition.

Supplementary Materials

The supplementary materials are available from the article webpage at https://doi.org/10.47852/bonviewJOPR62029619.

References

[1] Khonina, S. N., Kazanskiy, N. L., Butt, M. A., & Karpeev, S. V. (2022). Optical multiplexing techniques and their marriage for on-chip and optical fiber communication: A review. *Opto-Electronic Advances*, *5*(8), 210127. https://doi.org/10.29026/oea.2022.210127

[2] Salahdine, F., Han, T., & Zhang, N. (2023). 5G, 6G, and Beyond: Recent advances and future challenges. *Annals of Telecommunications*, *78*(9–10), 525–549. https://doi.org/10.1007/s12243-022-00938-3

[3] Quack, N., Takabayashi, A. Y., Sattari, H., Edinger, P., Jo, G., Bleiker, S. J., . . . , & Bogaerts, W. (2023). Integrated silicon photonic MEMS. *Microsystems & Nanoengineering*, *9*(1), 27. https://doi.org/10.1038/s41378-023-00498-z

[4] Xiao, Z., Liu, W., Xu, S., Zhou, J., Ren, Z., & Lee, C. (2023). Recent progress in silicon-based photonic integrated circuits and emerging applications. *Advanced Optical Materials*, *11*(20), 2301028. https://doi.org/10.1002/adom.202301028

[5] Ma, Y., Liu, W., Liu, X., Wang, N., & Zhang, H. (2024). Review of sensing and actuation technologies—From optical MEMS and nanophotonics to photonic nanosystems. *International Journal of Optomechatronics*, *18*(1), 2342279. https://doi.org/10.1080/15599612.2024.2342279

[6] Choi, D., Park, Y. J., Her, M. J., & Han, S. (2025). MEMS actuators for tunable waveguide devices in photonic integrated circuits: A brief review. *Current Optics and Photonics*, *9*(3), 185–195. https://doi.org/10.1364/COPP.9.000185

[7] Korček, R., Cheben, P., Fraser, W., Schmid, J. H., Milanizadeh, M., Alonso-Ramos, C., . . . , & Benedikovič, D. (2023). Low-loss grating coupler based on inter-layer mode interference in a hybrid silicon nitride platform. *Optics Letters*, *48*(15), 4017–4020. https://doi.org/10.1364/OL.495371

[8] Guo, L., Yin, X., Wu, Y., Wang, Y., Wang, L., Zhang, J., . . . , & An, J. (2025). Design and fabrication of SiN AWGs on an SOI platform. *Journal of Optics. Advance online publication*. https://doi.org/10.1007/s12596-025-02695-7

[9] Mondal, H., Goswami, K., Datta, T., Bose, R., Roy, S., & Sharma, A. (2023). All-optical demultiplexer: A review on recent research and developments. *Brazilian Journal of Physics*, *53*(4), 93. https://doi.org/10.1007/s13538-023-01315-8

[10] Zou, J., Sun, F., Wang, C., Zhang, M., Wang, J., Lang, T., . . . , & He, J.-J. (2022). Silicon-Based Arrayed waveguide gratings for WDM and spectroscopic analysis applications. *Optics & Laser Technology*, *147*, 107656. https://doi.org/10.1016/j.optlastec.2021.107656

[11] Gebregiorgis, Y., Chandran, S., Papadovasilakis, M., Bian, Y., Rakowski, M., Aboketaf, A., . . . , & Viegas, J. (2023). Straight and curved distributed Bragg reflector design for compact WDM filters. *Optics Express*, *31*(7), 11519–11535. https://doi.org/10.1364/OE.485609

[12] Zhang, Z., Zhang, S., Liu, X., Wei, Z., Sharma, T., Murugan, G. S., . . . , & Cheng, Z. (2025). Integrated optical spectrometers on silicon photonics platforms. *Laser & Photonics Reviews*, *19*(7), 2400155. https://doi.org/10.1002/lpor.202400155

[13] Cheben, P., Delâge, A., Janz, S., & Xu, D. (2010). Echelle and arrayed waveguide gratings for WDM and spectral analysis. In A. T. Friberg & R. Dändliker (Eds.), *Advances in information optics and photonics* (pp. 599–632). SPIE Press. https://doi.org/10.1117/3.793309.ch29

[14] Pottier, P., Strain, M. J., & Packirisamy, M. (2014). Integrated microspectrometer with elliptical Bragg mirror enhanced diffraction grating on silicon on insulator. *ACS Photonics*, *1*(5), 430–436. https://doi.org/10.1021/ph400165j

[15] Li, K., Zhu, J., Mao, Y., Zhang, N., & Hou, X. (2020). Design of efficient concave diffraction grating on 220 nm SOI platform for hybrid WDM-PDM (de)multiplexing. *Optics Communications*, *477*, 126358. https://doi.org/10.1016/j.optcom.2020.126358

[16] Li, H., Yin, Q., Jiang, K., Huang, R., & Qiu, W. (2026). Inverse design of high-performance concave diffraction gratings for demultiplexing via deep learning. *Optics Communications*, *603*, 132817. https://doi.org/10.1016/j.optcom.2025.132817

[17] Kharazmi, M., Pottier, P., Ozhikandathil, J., & Packirisamy, M. (2026). Air-gap-coupled MEMS-tunable Littrow SiN wavelength-division multiplexer. *Journal of the Optical Society of America B*, *43*(3), A175–A190. https://doi.org/10.1364/JOSAB.580808

[18] Hulyal, S. U., Hu, J., Wang, C., Cai, J., Lihachev, G., & Kippenberg, T. J. (2025). Arrayed waveguide gratings in lithium tantalate integrated photonics. *Optica*, *12*(7), 978–984. https://doi.org/10.1364/OPTICA.565570

[19] Tippinit, J., Kuittinen, M., & Roussey, M. (2023). Arrayed waveguide grating spectrometer on 2-µm-thick SOI platform. *EPJ Web of Conferences*, *287*, 01015. https://doi.org/10.1051/epjconf/202328701015

[20] Wen, J., Pan, Y., Wu, Z., & Zhang, Y. (2025). Ultra-compact wavelength multiplexer/demultiplexer based on subwavelength grating-assisted multimode interference coupler by inverse design. *Optoelectronics Letters*, *21*(9), 513–519. https://doi.org/10.1007/s11801-025-4115-8

[21] Gan, Z., Shevchenko, M., Nallaperuma Herzberg, S., & Savory, S. J. (2024). Fast neural network inverse model to maximize throughput in ultra-wideband WDM systems. *Optics Express*, *32*(22), 38642–38654. https://doi.org/10.1364/OE.536632

[22] Hsu, W.-C., Nujhat, N., Kupp, B., Conley, J. F., & Wang, A. X. (2023). On-chip wavelength division multiplexing filters using extremely efficient gate-driven silicon microring resonator array. *Scientific Reports*, *13*(1), 5269. https://doi.org/10.1038/s41598-023-32313-0

[23] Choi, B. K., Park, H., Kim, J. S., Ahn, S., Cho, S. Y., & Jeon, M. Y. (2024). Wavelength stabilization and intensity correction of fiber Fabry–Pérot tunable filter-based wavelength-swept laser. *IEEE Sensors Journal*, *24*(5), 6219–6227. https://doi.org/10.1109/JSEN.2024.3351849

[24] Fasihanifard, M., & Packirisamy, M. (2023). *Methods and systems of mechanical tuning multi channel optical components*. (U.S. Patent No. 20230384579A1). Google Patents https://patents.google.com/patent/US20230384579A1/en

[25] Ma, Y., Stewart, L., Armstrong, J., Clarke, I. G., & Baxter, G. (2021). Recent progress of wavelength selective switch. *Journal of Lightwave Technology*, *39*(4), 896–903. https://doi.org/10.1109/JLT.2020.3022375

[26] Chen, S., Zhang, Y., Hong, X., & Li, J. (2022). Technologies and applications of silicon-based micro-optical electromechanical systems: A brief review. *Journal of Semiconductors*, *43*(8), 081301. https://doi.org/10.1088/1674-4926/43/8/081301

[27] Lyu, Y. (2022). *Finite element method*. Singapore: Springer. https://doi.org/10.1007/978-981-19-3363-9

[28] Harvey, J. E., & Pfisterer, R. N. (2019). Understanding diffraction grating behavior: Including conical diffraction and Rayleigh anomalies from transmission gratings. *Optical Engineering*, *58*(8), 087105. https://doi.org/10.1117/1.OE.58.8.087105

[29] Mu, L., Wang, J., Ye, X., & Zhang, S. (2015). A weak Galerkin finite element method for the Maxwell equations. *Journal of Scientific Computing*, *65*(1), 363–386. https://doi.org/10.1007/s10915-014-9964-4

[30] Koh, D., Jung, Y., & Kim, J. (2026). Electrostatically actuated MEMS resonators for magnetic and electric field sensing: A review. *Microsystems & Nanoengineering*, *12*(1), 16. https://doi.org/10.1038/s41378-025-01128-6

How to Cite: Kharazmi, M., Pottier, P., Ozhikandathil, J., & Packirisamy, M. (2026). Optomechanical Response Analysis of a Tunable Monolithic Littrow WDM System Under Different Mechanical Boundary Conditions. *Journal of Optics and Photonics Research*. https://doi.org/10.47852/bonviewJOPR62029619